

Coulomb and electron-phonon interactions in metals

Igor S. Tupitsyn,^{1,2} Andrey S. Mishchenko,^{3,2} Naoto Nagaosa,^{3,4} and Nikolay Prokof'ev^{1,2,5}

¹*Department of Physics, University of Massachusetts, Amherst, MA 01003, USA*

²*Russian Research Center "Kurchatov Institute", 123182 Moscow, Russia*

³*Cross-Correlated Materials Research Group, RIKEN Advanced Science Institute (ASI), Wako 351-0198, Japan*

⁴*Department of Applied Physics, The University of Tokyo, 7-3-1 Hongo, Bunkyo-ku, Tokyo 113, Japan*

⁵*Department of Theoretical Physics, The Royal Institute of Technology, Stockholm SE-10691 Sweden*

(Dated: September 21, 2018)

An accurate and consistent theory of phonons in metals requires that all long-range Coulomb interactions between charged particles (electrons and ions) be treated on equal footing. So far, all attempts to deal with this non-perturbative system were relying on uncontrolled approximations in the absence of small parameters. In this work, we develop the Diagrammatic Monte Carlo approach for a two-component Coulomb system that obtains the solution to this fundamental problem in an approximation free way by computing vertex corrections from higher-order skeleton graphs. The feasibility of the method is demonstrated by calculating the spectrum of longitudinal acoustic phonons in a simple cubic lattice, determining their sound velocity, and obtaining the phonon spectral densities by analytic continuation of the Matsubara Green's functions. Final results are checked against the lowest-order fully self-consistent GW-approximation in both adiabatic and non-adiabatic regimes.

PACS numbers: 71.38.-k, 31.15.A-, 71.38.Mx

Standard theory of electron-phonon interaction (EPI) in metals involves a number of approximations. While some of them are based on the small adiabatic parameter $\gamma = \omega_D/\epsilon_F \sim \sqrt{m/M} \ll 1$ (where ω_D is the Debye frequency, ϵ_F is the Fermi energy, m and M are the electron and ion masses, respectively), other approximations, such as neglecting (i) vertex corrections based on the effective electron-electron interaction and (ii) the mutual self-consistent feedback between the phonon and electron subsystems, remain uncontrolled. Both effects do not involve small parameters because EPI in metals is inseparable from strong Coulomb forces between the electrons. Indeed, at the level of the *bare* Hamiltonian, unscreened Coulomb ion-ion interactions prevent formation of longitudinal acoustic phonons by shifting their frequencies all the way up to the frequency of ionic plasma oscillations, $\omega_p = q\sqrt{(4\pi e^2/q^2\epsilon_\infty)(n_e/M)} \equiv \sqrt{4\pi n_e e^2/M\epsilon_\infty}$, where $n_e = n_i$ is the conduction electron/ion charge density and ϵ_∞ is the ion-core dielectric constant. Once *both* the long-range electron-phonon and electron-electron interactions are accounted for, the acoustic spectrum is recovered back due to screening [1]; the underlying mechanism can be illustrated by replacing $4\pi e^2/q^2$ with $4\pi e^2/(q^2 + \kappa^2)$ (where κ is the Thomas-Fermi wavevector) in the phonon spectrum to get $\omega(q \rightarrow 0) \rightarrow \omega_p(q/\kappa)$.

In the adiabatic approximation it is assumed that interactions between (and with) the heavy ions are screened by the static dielectric function of a metal and the phonon spectrum is determined from the corresponding dynamic matrix of a solid. Thus transformed crystal vibrations and EPI are no longer singular at small momenta. When further progress is made by separating effects of electron-electron and electron-phonon interactions [2, 3], double-counting is dealt with by excluding static electronic

polarization terms from the renormalization of phonon propagators, and vertex corrections based on EPI are neglected because they are small in γ . The adiabatic approximation breaks down when $\gamma \gtrsim 1$ is considered, for instance, to explain enhancement of the critical temperature in phonon-mediated superconductors [4–6].

However, regardless of the γ parameter value, EPI does not involve natural small parameters in metals and remains strong. This means that even the first step in the adiabatic approximation (screening of long-range interactions) is ill-defined since the static dielectric function itself should be the outcome of the non-perturbative calculation based on all relevant interactions, including EPI. The importance of vertex corrections was studied by various groups in connection with superconducting [7–10] and Dirac [11] materials, as well as for polarons [12, 13], but never for a two-component Coulomb system in a systematic way when *all* forces are treated on an equal footing, and all uncertainties are quantified.

In this Letter, we develop the bold-line Diagrammatic Monte Carlo (BDMC) technique that allows us to deal with Coulomb interactions in a fully self-consistent, approximations free, manner and obtain final results with controlled accuracy by accounting for vertex corrections from higher-order skeleton diagrams. We demonstrate that BDMC leads to a theory capable of solving the fundamental problem of the phonon spectrum in a metal at any γ , including the most difficult regime of $\gamma \sim 1$, i.e. when there are no small parameters of any kind.

Our model simulation considers a simple cubic lattice of vibrating ions coupled to conduction electrons, and aims at computing the spectrum of longitudinal phonons and their velocity of sound in the thermodynamic limit. We also perform spectral analysis of the phonon Mat-

subara Green's function in the most difficult parameter regime $\gamma \sim 1$. We show that vertex corrections to the lowest-order (GW) approximation significantly soften the sound velocity at $\gamma \gtrsim 1$, and reduce the amplitude of the giant Kohn anomaly at small γ . As far as we know, this kind of studies were not possible to perform in the past; none of the previous work for Coulomb systems was done at the level of high-order skeleton technique in the absence of small parameters.

System. We consider a lattice model of a metal defined by the Hamiltonian

$$H = H_{FH} + H_c + H_{ph} + H_{el-ph}, \quad (1)$$

where H_{FH} is the standard Fermi-Hubbard model parameterized by the n.n. hopping amplitude t (with the tight-binding dispersion relation $\epsilon(\mathbf{k})$), the on-site repulsion U , and the chemical potential μ . In what follows we use the lattice constant a and hopping t as units of length and energy, respectively.

The second term describes Coulomb electron-electron interaction, $H_c = \sum_{\mathbf{i} < \mathbf{j}, \sigma, \sigma'} V_c(\mathbf{r}_{ij}) n_{\mathbf{i}\sigma} n_{\mathbf{j}\sigma'}$, where $n_{\mathbf{i}\sigma} = a_{\mathbf{i}\sigma}^\dagger a_{\mathbf{i}\sigma}$ is the electron density operator for the spin component $\sigma = \uparrow, \downarrow$ on site \mathbf{i} (we employ standard second-quantization notations for creation and annihilation operators), and $V_c(\mathbf{r}_{ij}) = U_c/|\mathbf{i} - \mathbf{j}|$; in Fourier space, $V_c(q \rightarrow 0) = 4\pi U_c/q^2$. We consider $U_c = e^2/\epsilon_\infty$ as an independent (from U) parameter; the bare electron-electron interaction is defined as the sum of local (spin-dependent) and non-local terms: $V_{ee}(\mathbf{r}_{ij}) = U\delta_{\mathbf{r}_{ij}} + V_c(\mathbf{r}_{ij})$ (for brevity, we do not explicitly mention the tensor structure of interactions, propagators, and irreducible objects in the spin space).

The Hamiltonian of ionic system is assumed to be harmonic and described by a collection of longitudinal phonons [14], $H_{ph} = \sum_{\mathbf{q}} \omega(\mathbf{q}) b_{\mathbf{q}}^\dagger b_{\mathbf{q}}$. Their bare spectrum is gapped at small momenta: $\omega(\mathbf{q} \rightarrow 0) = \omega_p$.

The electron-ion interaction has the standard density-displacement form,

$$H_{el-ph} = i \sum_{\mathbf{q}, \mathbf{k}, \sigma} M(\mathbf{q}) a_{\mathbf{q}+\mathbf{k}, \sigma}^\dagger a_{\mathbf{q}, \sigma} (b_{\mathbf{k}} + b_{-\mathbf{k}}^\dagger), \quad (2)$$

with the interaction vertex $M(\mathbf{q})$ based on the derivative of the Coulomb electron-ion potential. Since in all expressions we *always* have to deal with $|M(\mathbf{q})|^2$, it makes sense to introduce $V_{ep}(\mathbf{q}) = |M(\mathbf{q})|^2$ whose asymptotic form $[\omega_p/2]V_c(q)$ at $q \rightarrow 0$ is unambiguously fixed by electro-neutrality of the system. Solely for the purpose of minimizing the number of model parameters, we confine ourselves to $\omega(\mathbf{q}) = \omega_p$ and $V_{ep}(r) = (\omega_p/2)V_{ee}(r)$ with $\omega_p/t = 0.5$.

Methodology. Our calculations are based on the so-called G^2W -expansion, see Fig.1(a), when irreducible (with respect to cutting one line) diagrams for self-energy Σ and polarization Π are expressed in terms of fully-dressed Green's functions, G , and screened effective in-

teractions, W , defined self-consistently through Dyson equations in the Matsubara frequency-momentum space:

$$G^{-1} = G_0^{-1} - \Sigma, \quad W^{-1} = \bar{V}^{-1} - \Pi. \quad (3)$$

Here $G_0^{-1} = i\omega_n + \mu - \epsilon(\mathbf{k})$ and $D_0^{-1} = [\omega_m^2 + \omega^2(\mathbf{q})]/2\omega(\mathbf{q})$, are the bare electron and phonon Green's functions, respectively. Their Matsubara frequencies are defined differently: for fermions, $\omega_n = 2\pi T(n + 1/2)$ with integer n ; for bosons, $\omega_m = 2\pi Tm$ with integer m . Within the G^2W -expansion framework, one has to combine the bare electron-electron potential with the phonon-mediated term to form the frequency-dependent potential $\bar{V} = V_{ee} - D_0 V_{ep}$ appearing in the second Dyson equation. This formulation is complete in a sense that exponential convergence of the skeleton sequences with increasing the diagram order leads to the final solution of the problem [15].

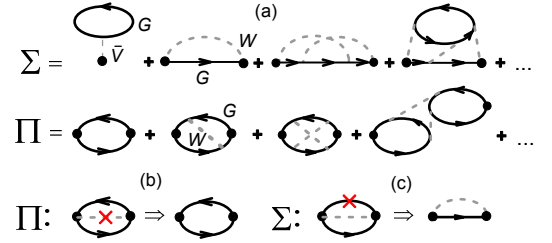


FIG. 1: (a) Skeleton (irreducible) diagrams for electron self-energy Σ and polarization function Π in terms of fully dressed Green's functions G and screened interactions W . Hartree term is the only graph based on the bare potential \bar{V} . (b-c) To go from free-energy diagrams to those for Π (b) or Σ (c), one has to remove the “measuring” line marked by the red cross.

To determine properties of the phonon subsystem, we define the polarization function irreducible with respect to cutting one phonon line, $\Pi_P^{-1} = \Pi^{-1} - V_{ee}$. By construction, in combination with V_{ep} , it plays the role of self-energy for the renormalized phonon propagator

$$D^{-1} = D_0^{-1} - \Sigma_{ph}; \quad \Sigma_{ph} = -V_{ep}\Pi_P. \quad (4)$$

Our implementation of the BDMC technique is closely following that described in Ref. [16]. We sample the configuration space of [17] skeleton free-energy diagrams in the (\mathbf{r}, τ) -representation with one of the lines always being marked (by red cross in Fig.1(b-c)) as “measuring”; its functional dependence on space-time coordinates of its end-points is arbitrary. When the “measuring line” is removed, the remaining diagram contributes either to Π , see Fig. 1(b), or to Σ , see Fig.1(c). In the imaginary-time representation, we need to split W into the sum of the bare electron-electron potential, $V_{ee}(\mathbf{r}_{ij})\delta(\tau_1 - \tau_2)$, and the rest, $W - V_{ee}(\mathbf{r}_{ij})\delta(\tau_1 - \tau_2)$, because δ -functional and generic functional dependencies on time are incompatible. This implies, in particular, that the measuring line cannot be of the V_{ee} -type [16].

Both Σ and Π are computed as sums of skeleton graphs, up to order N (there are $2N$ vertexes in the N -th order graph); we will denote these sums as Σ_N and Π_N . The lowest-order contributions are known right away because they are nothing but products of G and W functions; in the skeleton formulation, Σ_1 and Π_1 are equivalent to the GW-approximation with fully self-consistent treatment of the EPI feedback on polarization. By charge neutrality, Hartree terms involving $V_c(\mathbf{r} \neq 0)$ have to be removed. Thus, Monte Carlo statistics has to be collected only from higher-order diagrams and then added to the GW-result. The self-consistency loop is closed after Σ and Π are used in Dyson equations to define new G and W functions that are subsequently considered in all diagrams as the simulation continues. To solve Dyson equations (3-4) we employ Fast-Fourier-Transform algorithms to go to the momentum-frequency space where these equations are algebraic.

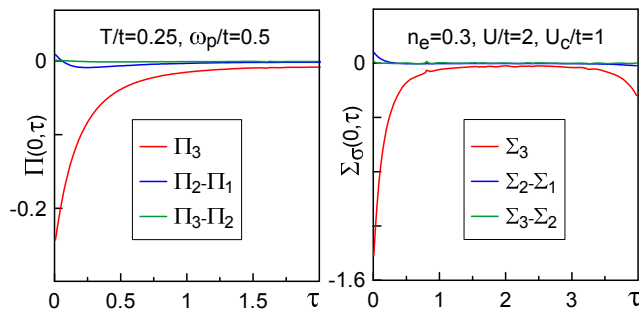


FIG. 2: Convergence properties of the skeleton sequence for system size $L = 16$ (other parameters are specified in the legends). In the left panel the local polarization $\Pi(0, \tau) = \sum_{\sigma} \Pi_{\sigma\sigma}(r = 0, \tau)$ and its order-by-order contributions are shown as functions of τ to demonstrate that Π_3 result (red line) is an order of magnitude larger than its partial contribution from diagrams of the second order (blue); third-order diagrams make an even smaller contribution (green line). In the right panel an identical analysis is presented for local self-energy $\Sigma_{\sigma}(0, \tau) = \Sigma_{\uparrow}(0, \tau) = \Sigma_{\downarrow}(0, \tau)$, with the same color scheme meaning.

The largest system size simulated in this work was $L^3 = 64^3$, with periodic boundary conditions. The thermodynamic limit was recovered by extrapolating results obtained for $L = 16, 32$, and 64 to infinity. We also have to perform an extrapolation to the $N \rightarrow \infty$ limit, or observe good convergence of results with increasing N . In two panels of Fig.2 we plot local polarization $\Pi(r = 0, \tau)$ and self-energy $\Sigma_{\sigma}(r = 0, \tau)$ along with their partial order-by-order contributions. Clearly, contributions from the third-order skeleton graphs are already very small, but understanding their role is required for estimating accuracy limits of calculations truncated at $N = 2$.

Results. The tight-binding model on a simple cubic lattice at half-filling satisfies the “nesting” condition at momentum $\mathbf{Q}_N = (\pi, \pi, \pi)$. This leads to singularity in

the density of states, logarithmic divergence of polarization at zero temperature, $\Pi(\mathbf{q} \rightarrow \mathbf{Q}_N) \sim \ln|\mathbf{q} - \mathbf{Q}_N|$, and the corresponding “giant” Kohn anomaly in the phonon spectrum (typical for one-dimensional systems) [18]. It is expected then that at low temperature the phonon spectrum is anomalously soft at \mathbf{Q}_N and there is a structural phase transition with the dominant density modulation at \mathbf{Q}_N . In contrast, the conventional Kohn anomaly is linked to the logarithmic divergence of the polarization derivative $\partial\Pi/\partial q$ at momentum transfer $\mathbf{q} = 2\mathbf{k}_F$ (at $T = 0$).

In Fig. 3 we show the dramatic temperature dependence of the renormalized phonon dispersion $\Omega(\mathbf{q})$ (along the $\langle 111 \rangle$ direction) at half-filling. The spectrum was deduced from the pole-approximation $D^{-1} \propto \omega^2 - \Omega^2(\mathbf{q})$ for the phonon propagator, see Eqs.(4). As temperature decreases, the cusp at \mathbf{Q}_N is getting more pronounced and the phonon spectrum softens; temperature scales (and appropriate system sizes) required for studying the structural transition point are exponentially small (large) in this case. Vertex corrections substantially reduce the amplitude of the Giant Kohn anomaly, see inset in Fig. 3, but do not eliminating it. Within the GW-approximation the phonon spectrum goes unstable at $T \lesssim 0.03$.

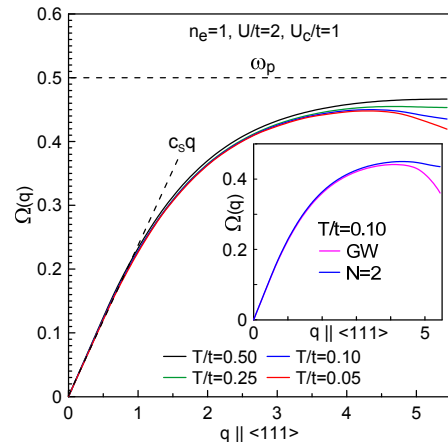


FIG. 3: Giant Kohn anomaly in the renormalized phonon spectrum $\Omega(\mathbf{q})$ at the nesting vector $\mathbf{Q}_N = (\pi, \pi, \pi)$ for $L = 32$, $n_e = 1$, and $N = 2$. In the inset we show how $\Omega(\mathbf{q})$ at $T/t = 0.1$ depends on the diagram order: GW-approximation (magenta), $N = 2$ (blue).

Away from half-filling, the phonon spectrum should demonstrate the standard Kohn anomaly at $q = 2k_F$ smeared by finite-temperature effects. It can be seen as a small wiggle on the phonon dispersion curve corresponding to density $n_e = 0.7$ in the momentum interval $4.5 < q < 5$ (at this filling factor, $k_F \approx 2.4$ along the $\langle 111 \rangle$ direction), see the main plot in Fig.4.

As far as screening effects are concerned, the plasmon gap at $q \rightarrow 0$ is closed at all densities, and $\Omega(\mathbf{q} \rightarrow 0)$ clearly demonstrates the characteristic sound-wave dependence $c_s q$, see Figs. 3 and 4. When n_e decreases (at constant U_c and ω_p this implies that ions are getting

lighter, $M = (4\pi U_c/\omega_p^2)n_e$) the spectrum at large values of $q > 2k_F$ saturates at ω_p , see the main panel in Fig.4, and the sound velocity increases, see Fig.4 inset. This behavior is in complete agreement with the Fermi-liquid theory prediction $c_s \propto (k_F/m)\sqrt{m/M} \propto n_e^{-1/6}$ at constant plasma frequency.

Near half-filling, $0.5 < n_e < 1$, where the adiabatic parameter is small, $\gamma \lesssim 0.1$, the effect of higher-order vertex corrections on sound velocity appears to be small, and phonon spectra at small momenta are indistinguishable within the error bars (this is not the case for large momenta, especially at \mathbf{Q}_N , see the inset in Fig.3). As expected, higher-order diagrams start playing a role at low density when the adiabatic parameter is approaching unity. In the inset of Fig.4 we show how the sound velocity depends on γ and how strong the effect of vertex corrections is. At densities $n_e \lesssim 0.2$ (or $\gamma \gtrsim 0.2$) the GW-approximation becomes rather unsatisfactory.

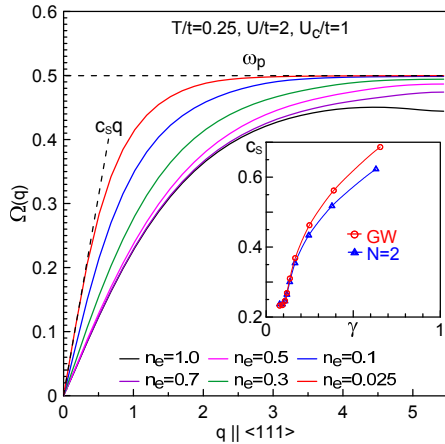


FIG. 4: Renormalized phonon dispersion $\Omega(\mathbf{q})$ along the $\langle 111 \rangle$ direction for various electron densities at $T = \omega_p/2 = 0.25t$. All results were obtained for $L^3 = 64^3$ and $N = 2$. Inset: sound velocity as a function of γ within the GW-approximation (red) and with $N = 2$ vertex corrections (blue). Both curves are extrapolated to the thermodynamic limit from the $L = 16, 32, 64$ set. Error bars are smaller than symbol sizes.

To gain additional information on dynamic properties of phonons, we perform analytic continuation of the Matsubara Green's function $D(\mathbf{q}, \tau)$ (with $\Pi(q = 0, \omega_m) \propto \delta_{m,0}$ obeying the particle conservation law requirement) into the real frequency domain. This is done by a combination of the unbiased stochastic optimization and consistent constraints methods [19, 20]. In Fig.5 we show the phonon spectral function for several values of momenta along the $\langle 111 \rangle$ direction at $T = \omega_p/2 = 0.25t$, and compare GW with $N = 2$ results. This is done in the most difficult low-density limit $n_e = 0.025$ where $\gamma \sim 1$. Note the large width of phonon peaks that is often comparable to their energies. Strong damping of longitudinal phonons is an inevitable property accompanying screening of long range interactions, which has been observed

in metals since early neutron scattering experiments [21]. First, the phonon damping is increasing with q at small momenta, but then the phonon lines are getting more narrow at larger values of q as the phonon life-time is becoming longer. For the three largest values of $q > 2k_F$, the phonon energy (first moment of the spectral function) saturates at ω_p , in accordance with Fig.4.

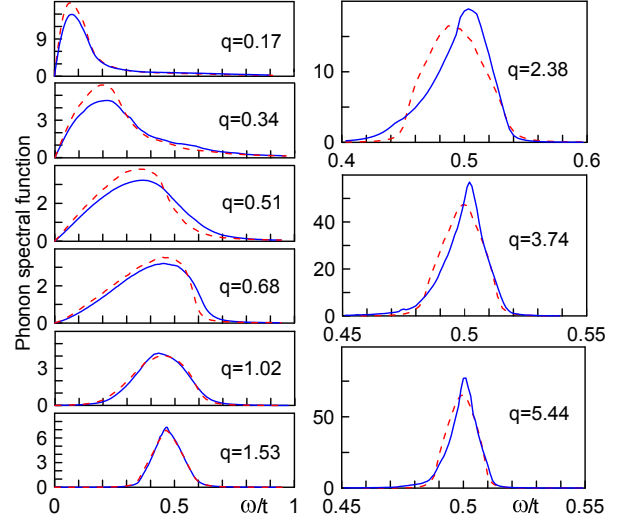


FIG. 5: Phonon spectral functions within the GW (blue solid lines) and $N = 2$ (red dashed lines) approximations at $T = 0.25t$ and $n_e = 0.025$ for $L^3 = 64^3$.

Conclusions. We developed and applied the BDMC approach to solve for electronic and vibrational properties of a metal in a fully self-consistent approximations free way by dealing with all Coulomb interactions on equal footing in the absence of small parameters. We find that the skeleton sequence converges fast for our parameters, and if final results are desired with accuracy of the order of one percent then it is sufficient to account only for the lowest-order vertex corrections in most cases. To arrive at this conclusion, we had to quantify the contributions from higher-order graphs. The presented field-theoretical framework allows one to address virtually any question about system's statistical behavior.

We demonstrated that our calculations capture the essence of screening effects in metals, and allow precise calculations of the renormalized phonon spectrum and sound velocity for all values of γ . In this work we focused on basic principles and discussed only the longitudinal acoustic phonons; including other phonon branches is left for future work but we do not see any difficulty in this regard. One may also quantify the feedback of the phonon subsystem on electronic properties (spectrum, dielectric function, optical conductivity, effective interactions, etc.) and aim at computing the irreducible Cooper-channel couplings. It would be equally interesting to investigate the relative effect of the on-site repulsion U on all quantities.

Acknowledgements. We thank B. Svistunov for dis-

cussions. This work was supported by the Simons Collaboration on the Many Electron Problem, the National Science Foundation under the grant PHY-1314735, the MURI Program “New Quantum Phases of Matter” from AFOSR, the Stiftelsen Olle Engkvist Byggmästare Foundation, and the Swedish Research Council grant 642-2013-7837. N.N. and A.S.M. are supported by Grant-in-Aids for Scientific Research (S) (No. 24224009) from the Ministry of Education, Culture, Sports, Science and Technology (MEXT) of Japan, and by ImPACT Program of Council for Science, Technology and Innovation (Cabinet office, Government of Japan).

-
- [1] E.G. Brovman and Yu. Kagan, JETP **52**, 557 [Sov. Phys. JETP **25**, 365] (1967).
 - [2] A.B. Migdal, JETP **34**, 1438 [Sov. Phys. JETP **7**, 996] (1958).
 - [3] G.M. Eliashberg, JETP **38**, 966 [Sov. Phys. JETP **11**, 696] (1960).
 - [4] E. Cappelluti, S. Ciuchi, C. Grimaldi, L. Pietronero, and S. Strässler, Phys. Rev. Lett. **88**, 117003 (2002).
 - [5] P. Paci, E. Cappelluti, C. Grimaldi, L. Pietronero, and S. Strässler, Physica C, 408-410, 240 (2004).
 - [6] S. Pisana, M. Lazzeri, C. Casiraghi, K. S. Novoselov, A. K. Geim, A. C. Ferrari and F. Mauri, Nat. Mater. **6**, 198 (2007).
 - [7] C. Grimaldi, L. Pietronero, and S. Strässler, Phys. Rev. Lett. **75**, 1158 (1995).
 - [8] E. Cappelluti and L. Pietronero, Phys. Rev. B **53**, 932 (1996).
 - [9] Z.B. Huang, W. Hanke, E. Arrigoni, and D.J. Scalapino, Phys. Rev. B **68**, 220507(R) (2003).
 - [10] J. Bauer, J. E. Han, and O. Gunnarsson, Phys. Rev. B **84**, 184531 (2011); Phys. Rev. B **87**, 054507 (2013).
 - [11] Bitan Roy, Jay D. Sau, and S. Das Sarma, Phys. Rev. B **89**, 165119 (2014).
 - [12] M. Capone and S. Ciuchi, Phys. Rev. Lett. **91**, 186405 (2003).
 - [13] A.S. Mishchenko, N. Nagaosa, and N. Prokofev, Phys. Rev. Lett. **113**, 166402 (2014).
 - [14] We do not consider transverse phonons in this work because they (i) do not contribute to the discussion of the fundamental role played by screening effects, (ii) introduce additional model parameters irrelevant for purposes of this study, and (iii) are trivial to include in the proposed numerical scheme.
 - [15] R. Rossi, F. Werner, N. Prokof'ev, and B. Svistunov, Phys. Rev. B **93**, 161102(R) (2016).
 - [16] S. A. Kulagin, N. Prokofev, O. A. Starykh, B. V. Svistunov, and C. N. Varney, Phys. Rev. Lett. **110**, 070601 (2013); Phys. Rev. B **87**, 024407 (2013).
 - [17] To have in place an efficient (diagram order independent) mechanism for verifying that the graph is irreducible, each line is assigned an auxiliary “momentum” and the momentum conservation law is enforced at each vertex. In irreducible graphs no two lines carry the same momentum—this can be quickly established with the help of the hash-table trick.
 - [18] W. Kohn, Phys. Rev. Lett. **2**, 393 (1959).
 - [19] A. S. Mishchenko, N. V. Prokofev, A. Sakamoto, and B. V. Svistunov, Phys. Rev. B **62**, 6317 (2000).
 - [20] N. Prokofiev, B. Svistunov, JETP Lett. **97**, 747 (2013).
 - [21] B. N. Brockhouse and A. T. Sewart, Phys. Renv. **100**, 756 (1955).